Detection of a SARS-CoV-2 sequence with genosensors using data analysis based on information visualization and machine learning techniques

Juliana Coatrini Soares[1], Andrey Coatrini Soares[2], Valquiria Cruz Rodrigues[1], Pedro Ramon Almeida Oiticica[1], Paulo Augusto Raymundo-Pereira[1], José Luiz Bott-Neto[1], Lorenzo Antonio Buscaglia[1], Lucas Daniel Chiba de Castro[1], Lucas Correia Ribas[1,3], Leonardo Scabini[1], Laís Canniatti Brazaca[4,5], Daniel Souza Correa[2], Luiz Henrique Capparelli Mattoso[2], Maria Cristina Ferreira de Oliveira[3], André Ponce Leon. Ferreira Carvalho[3], Emanuel Carrilho[4,5], Odemir M. Bruno[1], Matias Eliseo Melendez[6], Osvaldo N. Oliveira Jr[1*].

[1] São Carlos Institute of Physics (IFSC), University of São Paulo (USP), 13566-590 São Carlos, SP, Brazil.

[2]Nanotechnology National Laboratory for Agriculture (LNNA), Embrapa Instrumentação, 13560-970 São Carlos, SP, Brazil.

[3]Institute of Mathematics and Computer Sciences (ICMC), University of São Paulo (USP), 13566-590 São Carlos, SP, Brazil.

[4]São Carlos Institute of Chemistry (IQSC), University of São Paulo (USP), 13566-590 São Carlos, SP, Brazil.

[5]National Institute of Science and Technology in Bioanalytics – INCTBio, 13083-970 Campinas, SP, Brazil

[6]Pelé Little Prince Research Institute, Little Prince College, Little Prince Complex Curitiba, 80250-060 Curitiba, PR, Brazil

Corresponding Author: chu@ifsc.usp.br

Abstract

We report on genosensors to detect an ssDNA sequence from the SARS-CoV-2 genome, which mimics the GU280 gp10 gene (coding the viral nucleocapsid phosphoprotein), using four distinct principles of detection and treating the data with information visualization and machine learning techniques. Genosensors were fabricated on either gold (Au) interdigitated electrodes for electrical and electrochemical measurements or on Au nanoparticles on a glass slide for optical measurements. They contained a matrix of 11-mercaptoundecanoic acid (11-MUA) self-assembled monolayer (SAM) onto which a layer of capture probe (cpDNA) sequence was immobilized. Detection was performed using electrical and electrochemical impedance spectroscopies and localized surface plasmon resonance (LSPR). The highest sensitivity was reached with impedance spectroscopy, including using a low-cost (US$ 100) homemade impedance analyzer. Complementary ssDNA sequences were detected with a detection limit of 0.5 aM (0.3 copy/μL). This performance may be attributed to the high sensitivity of the electrical impedance technique combined with an appropriate arrangement of the sequences on the electrodes and hybridization between the complementary sequences, as inferred from polarization-modulated infrared reflection absorption spectroscopy (PM-IRRAS). The selectivity of the genosensor was confirmed by plotting the impedance spectroscopy data with a multidimensional projection technique (Interactive Document Mapping, IDMAP), where a clear separation was observed among the samples of the complementary DNA sequence at various concentrations and from buffer samples containing a non-complementary sequence and other DNA biomarkers. The diagnosis of SARS-CoV-2 mimicking sequences was also achieved with machine learning techniques applied to scanning electron microscope images taken from genosensors exposed to distinct concentrations of the complementary ssDNA sequences. In summary, the genosensors proposed here are promising for detecting SARS-CoV-2 genetic material (RNA) in biological fluids in point-of-care settings.

Keywords: COVID-19, SARS-CoV-2, genosensor, impedance spectroscopy, image processing, machine learning, localized surface plasmon resonance

1. Introduction

The challenges brought to humanity by the COVID-19 (Coronavirus disease 2019) pandemic have made it clear that low-cost and easily deployable methods are essential for clinical diagnosis (see, for instance, Mattioli et al. 2020[1]). Early diagnosis of the severe acute respiratory syndrome coronavirus 2 (SARS-CoV-2).[2,3] has been essential for pandemic management[4] and this is mostly performed by real-time polymerase chain reaction (RT-PCR).[5,6] Unfortunately, RT-PCR tests require several hours of sophisticated laboratory equipment and specialized professionals. The RT-PCR method is, therefore, inadequate for low-income countries or remote places with limited resources[7–9]. Other molecular technologies to detect genetic material such as LAMP (Loop-mediated isothermal AMPlification)[10] and CRISPR (Clustered Regularly Interspaced Short Palindromic Repeats)[11,12] suffer from similar limitations. Alternatively, serological tests using enzyme-linked immunosorbent assays (ELISA)[13,14] and immunosensors[15–17] detect antibodies produced by the infected person. It is worth mentioning that SARS-CoV-2 diagnosis by IgG/IgM screening is not sensitive in the first 1-2 weeks after initial infection, therefore incompatible with early diagnosis of just infected or asymptomatic patients. Hence, public policies to isolate the spreaders cannot rely on this type of test.

It seems that genosensors may be a long-term solution for mass testing of diseases requiring sensitive detection of genetic material. Genosensors are biosensors based on nucleic acid which detect ssDNA, RNA, hairpin DNA, nucleic acid aptamers, and locked nucleic acids (LNA), depending on the target molecule.[18] In fact, genosensors have long been used in research laboratories and other settings to diagnose various diseases, including SARS, as described in review papers[19–21]. However, these sensors have failed to reach the market with mass production, which could considerably

enhance the capability of managing this COVID-19 pandemic efficiently. For the SARS-CoV-2 virus, in particular, Mattioli et al.[1] discussed the many possibilities for genosensors, including point-of-care diagnosis. In our survey of the literature, we identified some sensors developed for SARS-CoV-2, but none of them relies on an electrical transducing principle. Optical detection of ssDNA SARS-CoV-2 sequences was reported with a detection limit of 0.22 pM by using localized surface plasmon resonance (LSPR) spectra[22]. In another work, optical detection of SARS-CoV-2 pseudovirus particles was demonstrated using a gold plasmonic nanocup array functionalized with antibodies, and sensitivity of 370 virus particles per mL.[23] Surface plasmon resonance (SPR) sensors were employed to detect nucleocapsid antibodies against SARS-CoV-2 with a detection limit of 1 μg/mL.[24] An effective diagnosis may be reached by detecting the spike protein of SARS-CoV-2, as it has been done using a field-effect transistor (FET)-based biosensor with a detection limit of 1.6×10^{1} pfu/mL and 2.42×10^{2} copies/mL for culture medium and clinical samples, respectively[25].

In this paper, we report on a genosensor produced with an active layer of immobilized single-strand DNA sequences (ssDNA) on a matrix of a self-assembled monolayer (SAM). Detection was performed with a complementary ssDNA sequence from the SARS-CoV-2 genome, which mimics the GU280 gp10 gene of the SARS-CoV-2 virus (coding the viral nucleocapsid phosphoprotein). An analysis of possible false positives was made using a non-complementary sequence and other non-related DNA sequences. Our primary purpose is to generate low-cost technology for point-of-care SARS-CoV-2 early diagnosis. We have therefore tested four different principles of detection, namely electrical, electrochemical impedance spectroscopy, LSPR, and image processing methods in conjunction with machine learning techniques.

2. Experimental section

2.1. Materials

The reagents were of analytical grade and used without further purification. Potassium chloride (KCl), sodium chloride (NaCl), magnesium chloride ($MgCl_2$), anhydrous sodium phosphate dibasic (Na_2HPO_4), anhydrous potassium phosphate monobasic (KH_2PO_4), anhydrous potassium ferricyanide ($K_3Fe(CN_6)$), and trihydrate potassium ferrocyanide ($K_3Fe(CN_6)$) were obtained from Synth (Brazil). *N*-(3-dimethylaminopropyl)-*N′*-ethylcarbodiimide hydrochloride (EDC), *N*-hydroxysuccinimide (NHS), ethanolamine and 11-mercaptoundecanoic acid (11-MUA) were purchased from Sigma-Aldrich (USA). High-purity deionized water (resistivity of 18.2 MΩcm) was obtained from a Milli-Q system (Millipore, USA). Experiments were performed at room temperature (~25°C). The SARS-CoV-2 cpDNA sequences used as a probe were synthesized by Sigma-Aldrich (Brazil), while the target complementary and non-complementary sequences were synthesized by Exxtend, Brazil. Phosphate buffered saline (PBS) solutions were prepared with 137×10^{-3}molL^{-1} NaCl, 10×10^{-3}molL^{-1} Na_2HPO_4, 1.7×10^{-3}molL^{-1} KH_2PO_4, and 2.7×10^{-3}molL^{-1} KCl (pH 7.4), with addition of 1.0×10^{-3}molL^{-1} $MgCl_2$ (PBS/$MgCl_2$ solution).

2.2 Fabrication of Electrodes

The Au interdigitated electrodes were produced using conventional photolithography at the Brazilian National Nanotechnology Laboratory (LMF/LNNano/CNPEM). They consisted of 50 pairs of 10 µm wide electrodes, 10 µm apart from each other, and were designed to exhibit a capacitive profile. For fabrication, BK7 glass slides were washed with a neutral detergent to remove impurities and rinsed

in ultrapure water, ethanol, and dried under nitrogen (N_2) gas flow. They were then treated with hexamethyldisiloxane (HMDSO) and positive photoresist AZ4210 deposited by spin coating during 10 and 30s, respectively. The electrodes were fabricated using a lithographic mask and exposed to UV light for 10s for photoresist polymerization followed by treatment with tetrabutylammonium. The slides were coated with 20nm of chromium as an adhesive layer, and then 150nm Au-layer with the sputtering system BA 510 (Balzers).

2.3 Preparation of genosensors

The Au interdigitated electrodes were coated with a self-assembled monolayer (SAM) of 11-mercaptoundecanoic acid (11-MUA) (5.0×10^{-3}molL^{-1}) during 24h in ethanol at room temperature. A solution of 100×10^{-3}mol L^{-1} EDC and 100×10^{-3}molL^{-1} NHS was used for 30 min at room temperature in water to increase the attachment of cpDNA probes to carboxylic groups of thiol sites. Then, these devices were immersed in a 1.0×10^{-3}molL^{-1}PBS/$MgCl_2$ solution (1.0×10^{-6}mol L^{-1}) containing the NH_2-DNA capture probe (cpDNA) for 12h at room temperature. The probe had the sequence 5'/5AmMC6/ATTTCGCTGATTTTGGGGTC (Sigma-Aldrich). These genosensors were used for the electrical and electrochemical impedance spectroscopy measurements.

2.4. Fabrication of optical genosensor device

The substrates used in the optical detection measurements (see Figure S1- a and Figure S1- b) were fabricated by ultrathin film deposition followed by thermal annealing. They consist of gold nanoparticles onto the surface of glass substrate (AuNp/glass) with an average size distribution of 40 nm in height and 130 nm in

diameter (Figure S1-c), according to atomic force microscopy (AFM) (Dimension Icon, Bruker) in the tapping mode. The LSPR spectrum has a peak absorption at ca. 570 nm (Figure S1-b) characterized using a Hitachi U-2900 spectrometer. The fabrication steps were as follows. Microscopy glass slides (Perfecta Lab, Brazil) with dimensions 25× 9 mm, 1.0 mm thick, were cleaned using an ultrasonic bath at 65°C with neutral detergent solution 1:10 v/v ratio for 20 min (Extran® MA02 from Merck Supelco) in ultrapure water during 10 min and in isopropanol 99.5% (Synth, Brazil) for 10 min. The substrates were treated using UV/ozone washing cleaning procedure for 15 min. The substrates were finally rinsed with isopropanol, ultrapure water and dried under a flow of nitrogen. A 15-nm thick film of gold was deposited by physical vapor deposition with growth rate 0.7 Å/s and chamber pressure 1×10^{-6}mBar, using MB-Evap inside a LabMaster 130 Glovebox (MBraun). The film thickness was controlled with a quartz crystal microbalance inside the evaporation chamber and confirmed with the Dektak 150 surface profiler (Veeco). The films were submitted to thermal annealing at 600 °C for 6 h in an oven (Mufla EDGCON 5P, EDG, Brazil). The substrates with gold nanoparticles were then cleaned in an ultrasonic bath with isopropanol and in ultrapure water for 10 min. The photography of the fabricated substrates and the characterization results are given in the supplementary information (Figure S1).

The plasmonic substrates were functionalized following the same protocol described to produce the Au interdigitated electrode genosensor. The first step was forming a SAM of 11-MUA by immersing the substrate in 10mM 11-MUA/ethanol solution for 12h at room temperature (25°C). The activation of the carboxyl end groups of 11-MUA was performed using 100×10^{-3}molL^{-1} EDC and 100×10^{-3}molL^{-1} NHS, resulting in a succinimide ester (-COOSuc) terminated layer on the surface of gold nanoparticles. The cpDNA SARS-CoV-2 probe was immobilized on the nanoparticles

by immersion in a solution containing the probe molecules at the 1.0×10^{-6}molL^{-1} concentration, diluted in 1.0×10^{-3}molL^{-1} PBS/$MgCl_2$ buffer solution, with 24 h incubation at 4°C.

2.5 Protocol of detection

Detection experiments were performed with complementary and non-complementary sequences in a concentration range between 1.0×10^{-18} and 1.0×10^{-6}molL^{-1} diluted in PBS/$MgCl_2$ solutions for the electrical and electrochemical measurements. The positive control for SARS-CoV-2 and negative control samples (Exxtend, Brazil) are given in Table 1.

Table 1. Sequences of cpDNA SARS-Cov-2 (probe), ssDNA SARS-CoV-2 positive control, and negative control used in this work

Type	Sequence
cpDNA SARS-Cov-2 (probe)	5'-5AmMC6/-ATTTCGCTGATTTTGGGGTC-3'
ssDNA SARS-CoV-2 positive control	5'-TGATAATGGACCCCAAAATCAGCGAAATGCACCCCGCATTACGTTTGGTGGACCCTCAGATTCAACTGGCAGTAACCAGA-3'
Negative Control	5' - CCCATCCTCACCATCATCACACTGGAAGACTCCAGTGGTAATCTACTGGGACGGAACAGCTTTGAGGTGCGGTTTGTG - 3'

The optimized hybridization process was performed at 85°C for 30 min, followed by placing the solution on ice for 5 min. For the impedance spectroscopy measurements, the genosensor was immersed in a solution with 300 µL of each one of the concentrations 1.0×10^{-18}, 1.0×10^{-16}, 1.0×10^{-14}, 1.0×10^{-12},1.0×10^{-10}, 1.0×10^{-8}, and 1.0×10^{-6} mol L^{-1}. Control experiments were performed to verify the selectivity of the genosensor, with measurements in DNA samples from *Staphylococcus aureus* (IDT, USA), human papillomavirus (HPV16) (Sigma-Aldrich, USA), *Agalactiae* (IDT, USA), and fetal bovine serum (Sigma-Aldrich, USA). Electrical impedance measurements were carried out with an impedance analyzer 1260A (Solartron Analytical), controlled by Smart software, in the frequency range from 1 Hz to 1 MHz, with d.c. potential 0 mV and a.c. potential 50 mV. Owing to the potential commercial application of SARS-CoV-2 detection in point-of-care settings, we also performed the electrical impedance analysis using the instrument Simple-Z^{TM} (Figure S2), which is a wide-spectrum, portable, and low-cost (~US$ 100) impedance spectrometer developed in-house. It employs the integrated circuit AD5933 (Analog Devices), which includes an alternate- and direct-current generator, a frequency synthesizer, an analog-to-digital converter (ADC), and a single-frequency discrete Fourier transform (DFT) multiply-accumulate core. To control the output signal amplitude and frequency and the sampling rate throughout the frequency range between 1 Hz and 100 kHz, Simple-Z^{TM} contains an external clock source, a potentiometer, and a digital-to-analog converter coupled with operational amplifiers (op-amps). For noise filtering and to avoid flattening and saturation issues in the ADC, the response signal amplitude is automatically regulated by an analog multiplexer (AMux), op-amps, ceramic capacitors, and thin-film resistors. Additional AMux shifts through calibration resistances to provide a reference DFT result. A micro-controller executes a C^{++} impedance spectroscopy algorithm, bridging

between the computer (USB communication) and the analog circuitry (I2C communication).

Electrochemical experiments were carried out in 5.0×10^{-3}molL^{-1} potassium-ferrocyanide and -ferricyanide ($K_3[Fe(CN)_6]/K_4[Fe(CN)_6]$) (Sigma-Aldrich) dissolved in 1.0×10^{-3}molL^{-1}PBS/$MgCl_2$ solution. The instrument employed was an electrochemical system PGSTAT302 (Metrohm Autolab) controlled by GPES 4.9.7 software. All measurements were carried out in a 25mL glass cell at 25°C, with a three-electrode configuration: Au interdigitated electrodes coated with a SAM of 11-MUA with a layer of the cpDNA SARS-CoV-2 (probe) as the working electrode, an Ag/AgCl (3 mol L^{-1}KCl) was used as a reference and a platinum foil (1.0cm^2) as an auxiliary electrode. The solution within the cell was neither stirred nor aerated during the measurements. Electrochemical impedance spectroscopy (EIS) data were acquired with the PGSTAT302 with a FRA2 algorithm in the frequency range between 0.1Hz and 100kHz with an amplitude of 10 mV and under open circuit potential (OCP) conditions.

The optical detection experiments were performed by transmission/absorption spectral measurements (Figure S3) before and after incubation of the genosensor with dilutions (in PBS/$MgCl_2$) containing complementary and non-complementary ssDNA SARS-CoV-2 positive control sequences at the molar concentrations 1.0×10^{-10}, 1.0×10^{-8}, 1.0×10^{-6}mol L^{-1} during 30 min at 85 °C followed by cooling in ice, rinsing with ultrapure water, and drying under a flow of N_2. The LSPR spectrum was acquired from 400 nm to 900 nm using a fiber optic spectrometerUSB4000 (Ocean Optics) and a tungsten halogen lamp LS-1 (Ocean Optics). All spectral measurements were averaged from 10 scans with 100 ms accumulation time. The acquired data were analyzed using programs developed in Python3.8. The shift in the LSPR peak was determined with an algorithm implemented using the library NumPy[26] and the package PeakUtils[27].

2.6. SEM images

Scanning electron microscopy (SEM) images were obtained with a Zeiss-LEO-440 electron microscope equipped with a detector 7060 (Oxford Instruments) and operating at 15 kV. Prior to the analysis, the genosensing units were affixed onto aluminum (Al) stubs and covered with a 3 nm Au layer deposited by sputter coating using a BAL-TEC MED 020 coating system for improved electrical contact and imaging. In order to collect a reliable and representative dataset, 10 images were acquired in duplicate from different regions of each sample. The total magnifications used in the SEM images were 10,000X and 1,000X, where the latter was chosen to coincide with the upper limit of optical microscopes. This analysis was carried out to verify the plausibility of using optical microscopes in the future for the same purpose. Typical SEM images of the genosensing units are shown in Figure 1.

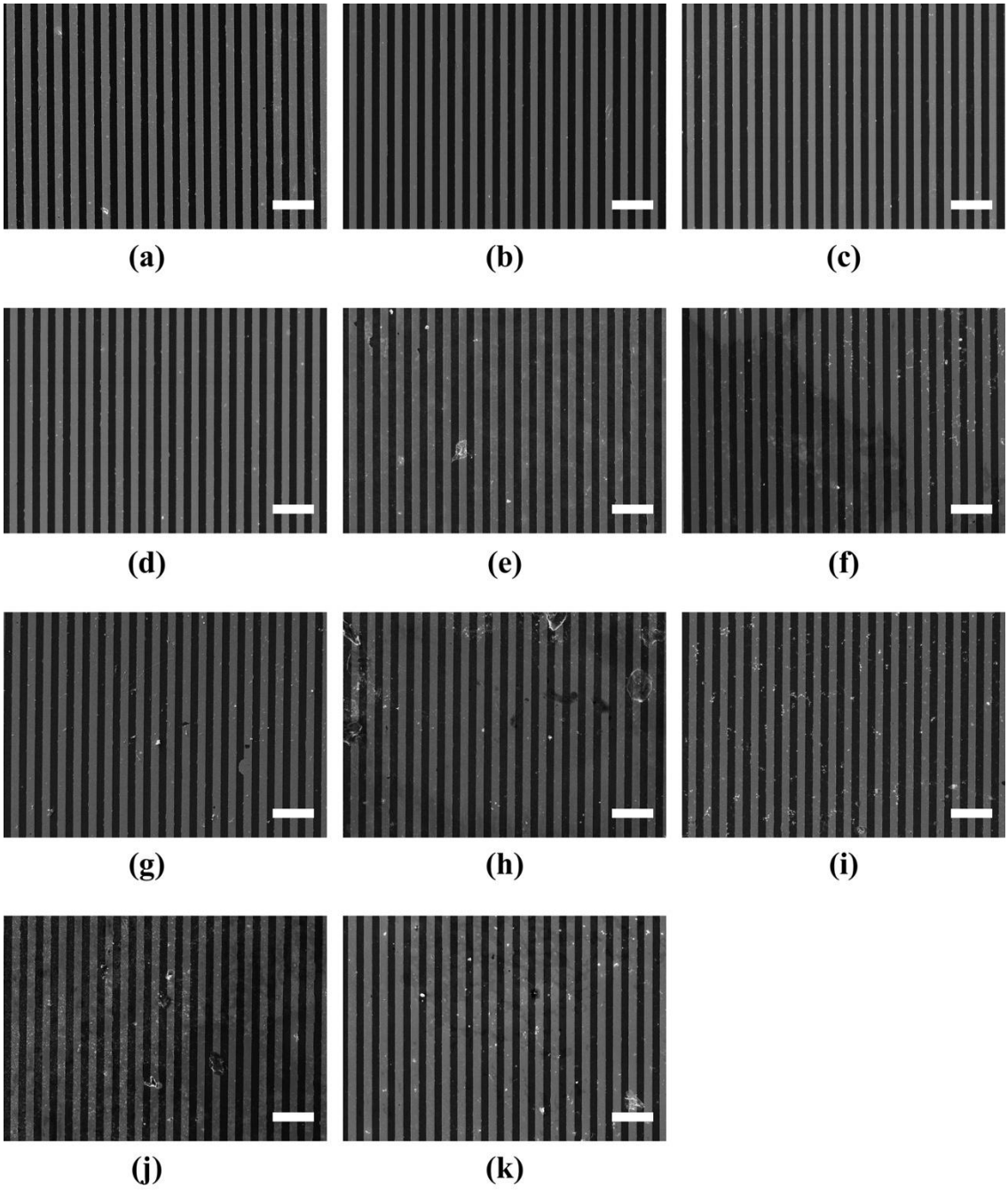

Figure 1. SEM images (1,000X) of the (a) blank control; genosensing units exposed to (b) negative control; (c) HPV16 interferent; (d) PCA3 interferent, and to different concentrations (mol L^{-1}) of the ssDNA SARS–CoV-2 positive control: (e) 10^{-18}mol L^{-1}; (f) 10^{-16} mol L^{-1}; (g) 10^{-14}mol L^{-1}; (h) 10^{-12}mol L^{-1}; (i) 10^{-10}mol L^{-1}; (j) 10^{-8}mol L^{-1}; (k) 10^{-6}mol L^{-1}. Scale bar: 50µm.

2.7. Mechanism behind SARS-CoV-2 Detection

The mechanism behind the detection of the SARS-CoV-2 sequence was elucidated using polarization-modulated infrared reflection absorption spectroscopy (PM-IRRAS), which also served to verify the film architecture of the genosensors. The measurements were performed with a spectrophotometer PMI 550 (KSV Instruments), with the Au electrode spectrum as a reference. The incident angle of the incoming IR beam was 81º, and the spectral resolution was 8 cm^{-1}. The PM-IRRAS signal was obtained from *s* and *p* reflectivity components through Eq. 1, where R_p and R_s are the parallel and perpendicular components to the plane of incidence of the IR light, respectively.

$$\frac{\Delta R}{R} = \frac{R_p - R_s}{R_p + R_s} \tag{1}$$

2.8. Data analysis with information visualization and machine learning

Dimensionality reduction of biosensing data is used to evaluate selectivity and the presence of false positives. Herein, electrical and electrochemical impedance spectra were processed with the multidimensional projection strategy referred to as Interactive Document Mapping (IDMAP).[28] The mapping strategy strives to reproduce, in a low-dimensional space, the relative pairwise proximities amongst the data samples observed in the original *n*-dimensional feature space (*n* is the number of measurements in a spectrum) by minimizing the error as in Eq. 2. The Euclidean distance $\delta(x_i, x_j)$ between any two samples $\mathbf{x_i} = (x_{i1}, x_{i2}, \ldots, x_{in})$ and $\mathbf{x_j} = (x_{j1}, x_{j2}, \ldots, x_{jn})$ is computed as a proxy of their dissimilarity, and the IDMAP strategy is applied to project the samples into a two-dimensional feature space, for visualization purposes. It produces a novel representation of samples $\mathbf{x_i}$ and $\mathbf{x_j}$ as $\mathbf{y_i} = (y_{i1}, y_{i2})$ and $\mathbf{y_j} = (y_{j1}, y_{j2})$. Eq. 2 expresses the error to be

minimized for a pair of samples $\mathbf{x_i}$ and $\mathbf{x_j}$, where $d(y_i, y_j)$ denotes the Euclidean distance computed in the reduced space, and δ_{max} and δ_{min} denote the maximum and minimum distance values between the data instances in the original representation space[29].

$$Error_{IDMAP} = \frac{\delta(x_i, x_j) - \delta_{\min}}{\delta_{\max} - \delta_{\min}} - d(y_i, y_j) \quad (2)$$

In the predictive analysis using machine learning techniques, a set of 350 images was employed, corresponding to sensing units subjected to either distinct concentrations of SARS–CoV-2, negative sequences, or interferents (HPV16 and PCA3). The latter samples are considered as control measurements, as indicated in Table 2. The images have 8-bit pixels (grayscale) and a resolution of 1024 × 714. The samples were taken with two magnifications (1,000X and 10,000X), allowing us to observe the effects of different scales. We considered two classification schemes, binary (positive or negative for SARS–CoV-2) and multiclass (separating different concentrations and control samples).

Table 2. Description of the SEM images, magnification, and the number of samples for each condition.

Analyte	Class Name (label)	1,000X	10,000X
Probe	negative (n)	30	10
HPV16	negative (interferent)	10	0
PCA3	negative (interferent)	10	0
[SARS–CoV-2] 10^{-6}mol L^{-1}	positive (6)	30	20
[SARS–CoV-2] 10^{-8}mol L^{-1}	positive (8)	20	20
[SARS–CoV-2] 10^{-10}mol L^{-1}	positive (10)	20	20
[SARS–CoV-2] 10^{-12}mol L^{-1}	positive (12)	20	20
[SARS–CoV-2] 10^{-14}mol L^{-1}	positive (14)	20	20
[SARS–CoV-2] 10^{-16}mol L^{-1}	positive (16)	20	20
[SARS–CoV-2] 10^{-18}mol L^{-1}	positive (18)	20	20

As the datasets are initially imbalanced concerning the number of examples in each class, in the classification step we apply a resampling process using 100 random configurations (i.e., 100 trials). This strategy ensures a uniform class distribution so that

at each iteration each class has the same number of samples, as shown in Table S1 in the Supporting Information. Two machine learning techniques were employed in a 2-step pipeline: (1) feature extraction and (2) classification. In the first step, image features were extracted using standard computer vision methods. The patterns within the images of the genosensing units are complex combinations of pixel intensity variations and spatial distribution. These patterns can be categorized as visual texture, a property studied in computer vision and image analysis since the 1970s. The texture analysis methods can be organized according to their underlying mathematical approach, such as statistical, model-based, spectral, agent-based, and neural network-based methods.[30] Since the performance of each technique and category may depend on the problem under analysis, herein we considered a set of distinct texture methods to recognize the genosensing images, covering both classical and recent approaches.

We employed recent Deep Convolutional Neural Networks (DCNN) and state-of-the-art methods for texture visual discrimination[31]. The following texture analysis methods were used: Gray Level Difference Matrix (GLDM)[32], Fourier descriptors[33], Complex Network Texture Descriptor (CNTD)[34], Fractal descriptors[35], Adaptive Hybrid Pattern (AHP)[36], Completed Local Binary Patterns (CLBP)[37] and Local Complex Features and Neural Network (LCFNN)[38]. We employed the following DCNN models: InceptionResNetV2[39], DenseNet[40], and MobileNet[41]. They are first pre-trained using the ImageNet dataset from the Large-Scale Visual Recognition Challenge[42], composed of around 1.2 million images belonging to 1,000 different visual categories. The models are then ported to our application as feature extractors through a transfer-learning process. We remove the final fully-connected layers and then apply a global average pooling (GAP)[43] to obtain image features from the last convolutional layer's output. The

DCNN can thus process images of any size greater than its predefined standard (usually 224 or 299), i.e., we do not need to rescale the SEM images. The original 8-bit pixel values are divided by 255, thus normalizing all values within the range [0,1]. In the experiments, we adopted the same parameter values described in the original paper of each method.

The image feature vectors obtained using the extractor methods were used in induced model classifiers employing the Support Vector Machine (SVM) (linear kernel)[44] and Linear Discriminant Analysis (LDA)[45] techniques (step 2). These classifiers are widely employed for classifying image features, justifying their choice, and led to the best results among those tested, which included Naive Bayes and KNN. In this step, we considered (i) a binary classification between the samples exposed to SARS–CoV-2 (as the positive class) and those either not exposed or exposed to HPV16 and PCA3 (as the negative class), and (ii) a multiclass classification that attempts to distinguish between the distinct SARS–CoV-2 concentrations, negative samples (zero) and with interferents (HPV16 and PCA3). In all experiments, the average accuracy and standard deviation of the 100 random trials were reported and used to evaluate the induced classifier predictive performance. The 10-fold cross-validation scheme was used in each trial to define the test and training subsets.[46] The image features were also used in an unsupervised analysis through the visual projection with t-distributed Stochastic Neighbor Embedding (t-SNE)[47] and the k-means clustering algorithm.

3. Results and discussion

Electrical detection

The genosensor made with a matrix based on 11-MUA was able to detect complementary (positive) sequences in the concentration range between 1.0×10^{-18} and 1.0×10^{-6} mol L^{-1} using impedance (Z) spectroscopy, as seen in the capacitance (C, Eq. 3) spectra in Figure 2. The specific interactions between the cpDNA SARS-CoV-2 and the positive sequence are sufficient to yield measurable differences in the relative capacitance, defined as the difference in capacitance with and without ssDNA SARS-CoV-2 (Positive Control). The distinction in the electrical response occurs mainly at low frequencies. According to Lvovich and MacDonald[48,49], the frequency-dependent electrical response in sensors is governed by three types of mechanism. At high frequencies, the electrical signal depends mostly on the electrode capacitance while at intermediate frequencies, between 1 kHz and 100 kHz, this response is related to changes at the sensor surface. At low frequencies (1 to 1000 Hz), the electrical double layer formed at the sensor/electrolyte (sample) interface governs the response. The results in Figure 2, therefore, indicate the relevance of double-layer effects in the detection.

$$C = \mathrm{Re}((j\omega Z)^{-1}) \qquad (3)$$

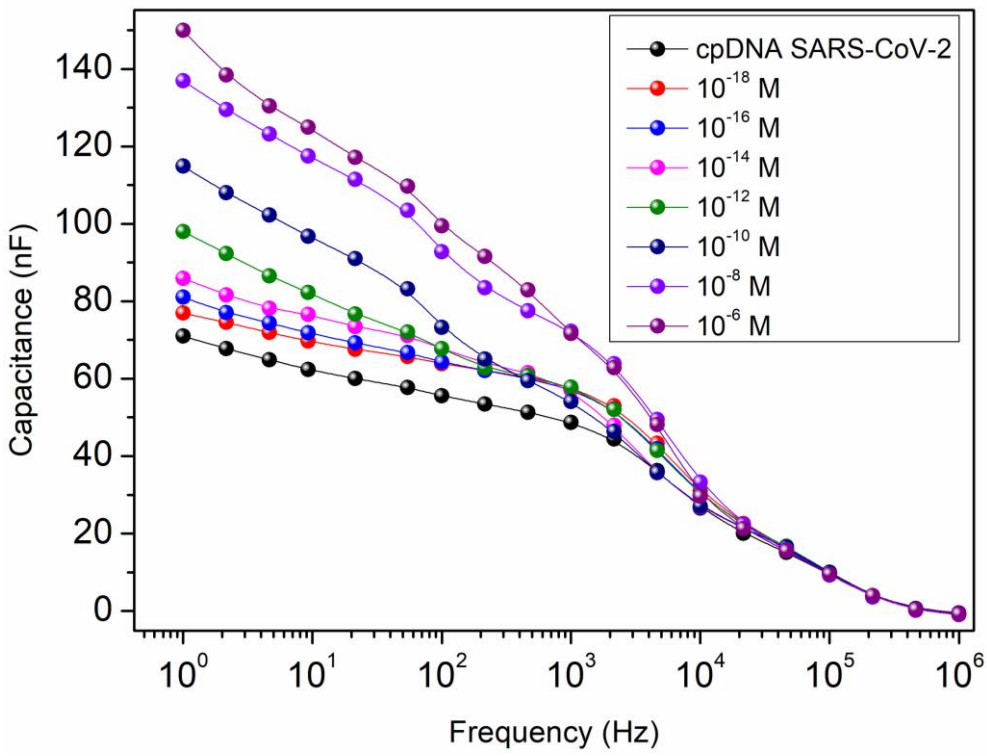

Figure 2. Capacitance spectra for detection of ssDNA SARS-CoV-2 in synthetic samples using a genosensor built with a matrix of 11-MUA SAM under an active layer containing the cpDNA SARS-CoV-2 (Probe).

For practical reasons, one may wish to display the results not in the form of spectra as in Figure 2, but with a single capacitance value at a given frequency. Measuring the signal at a single frequency would also facilitate displaying the detection results. We have therefore analyzed the capacitance spectra in Figure 2 with the Parallel Coordinates visualization technique[50] which is useful to reveal the frequencies responsible for the highest distinction of the different SARS-CoV-2 concentrations. Figure 3a shows a parallel coordinates plot of the capacitance data. The distinction ability is estimated with the Silhouette Coefficient metric (S) expressed in Eq. 4, where m refers to the total number of samples, a_i denotes the average distance between the i^{th} data point and the other data points in the same category as itself, and b_i is the smallest of the average distances computed between the i^{th} data point to the data points in each

category distinct from *i*. *S* varies in the range [−1,+1] and is useful as an estimate of the cohesion and separability of the different categories of samples. Here we computed its value at each frequency of the measured spectrum. Thus, *S*~1 indicates the signal at a given frequency is useful for distinction among the samples, while *S*~0 and *S*~−1 mean, respectively, that the signal is neutral or deleterious for such a distinction.[50,51] In Figure 3a, the values of *S* are encoded as small bars at the top of the axis relative to each measured frequency, color coded as follows: blue for positive values, white for *S* ~0, and red for negative values; the length of the filling is proportional to the value. Most frequencies are useful for detection, which leads to an overall *S* of 0.936 (for all ssDNA SARS-CoV-2 positive samples and frequencies), thus confirming the excellent distinguishing capability of the genosensor. Assessing the parallel coordinates plot in conjunction with the Silhouette coefficient (Eq. 4) is also useful to determine the best frequency at which a calibration curve can be taken. From the values estimated for *S*, we chose 1 Hz and the capacitance versus SARS-CoV-2 concentration in the logarithm scale is shown in Figure 3b. Taking the initial linear part of the curve, we obtained a detection limit of 0.5 aM using the IUPAC recommendations (Eq.5)[52] where SD is the standard deviation of 10 blank curves. This detection limit corresponds to 0.3 copies per µL, which is lower than values typically obtained using RT-PCR kits (1.25 copies per µL).[53] Hence, the genosensor may be applied to biological samples, though further studies are required to confirm whether the performance will remain in complex samples.

$$S = \frac{1}{n}\sum_{i=1}^{n}\frac{\left(b_i - a_i\right)}{\max\left(b_i, a_i\right)} \tag{4}$$

$$LOD = 3 \times SD \quad (5)$$

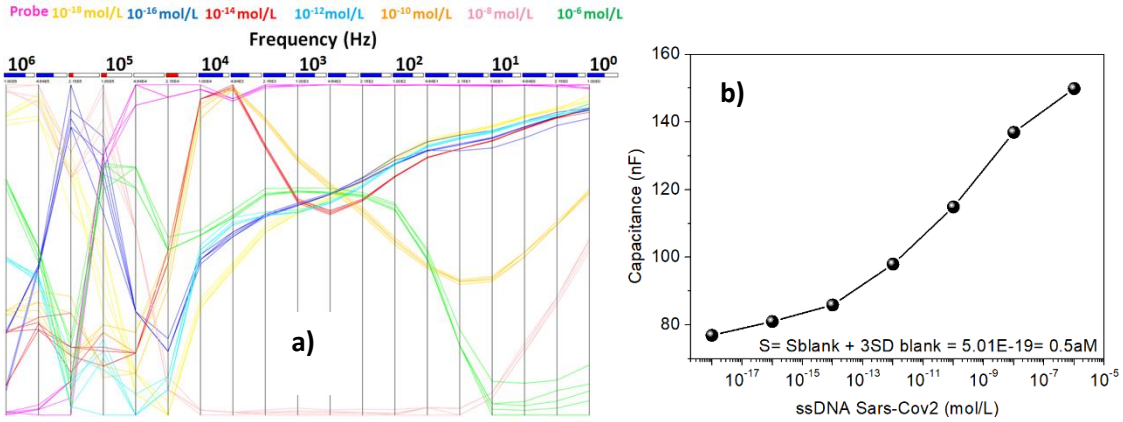

Figure 3.a) Parallel Coordinates (PC) plot for the data obtained with 11-MUA genosensor functionalized with an ssDNA SARS-CoV-2 probe. The angular frequencies are depicted in the horizontal axis, while the values mapped to the parallel axes correspond to the normalized capacitance values. b) Calibration curve with the capacitance at 1 Hz plotted versus the concentration of SARS-CoV-2 on a logarithm scale.

The high sensitivity of the genosensor was our first goal, but selectivity is also crucial. This capability was tested further with control experiments, in addition to the measurements with the non-complementary sequence at various concentrations. Because the comparison now involves tens of spectra, we plotted the capacitance data in Figure 4 with the multidimensional projection IDMAP. It is relevant that the spectra for the complementary sequence (positive for SARS-CoV-2) can be distinguished from those of negative sequences, from PBS, fetal bovine serum (FBS), and other DNA biomarkers such as DNA samples from *Staphylococcus aureus*, HPV16, and *Agalactiae*. We also verified whether detection was possible in the absence of the probe sequence and if incorporation of ethanolamine would hinder non-specific adsorption and thus enhance the sensitivity and selectivity. The map in Figure S4 in the Supporting Information suggests that ethanolamine has a deleterious effect, as the distinguishing

ability of the corresponding genosensor is considerably lower. The distinction was also poor in the absence of the cpDNA SARS-CoV-2, as one could expect. In subsidiary experiments, we verified that positive sequences of SARS-CoV-2 could be detected in impedance spectroscopy measurements performed with the homemade Simple-Z^{TM} instrument, as demonstrated in the IDMAP plot in Figure S2. This approach is promising for making the genosensors available in point-of-care diagnosis systems.

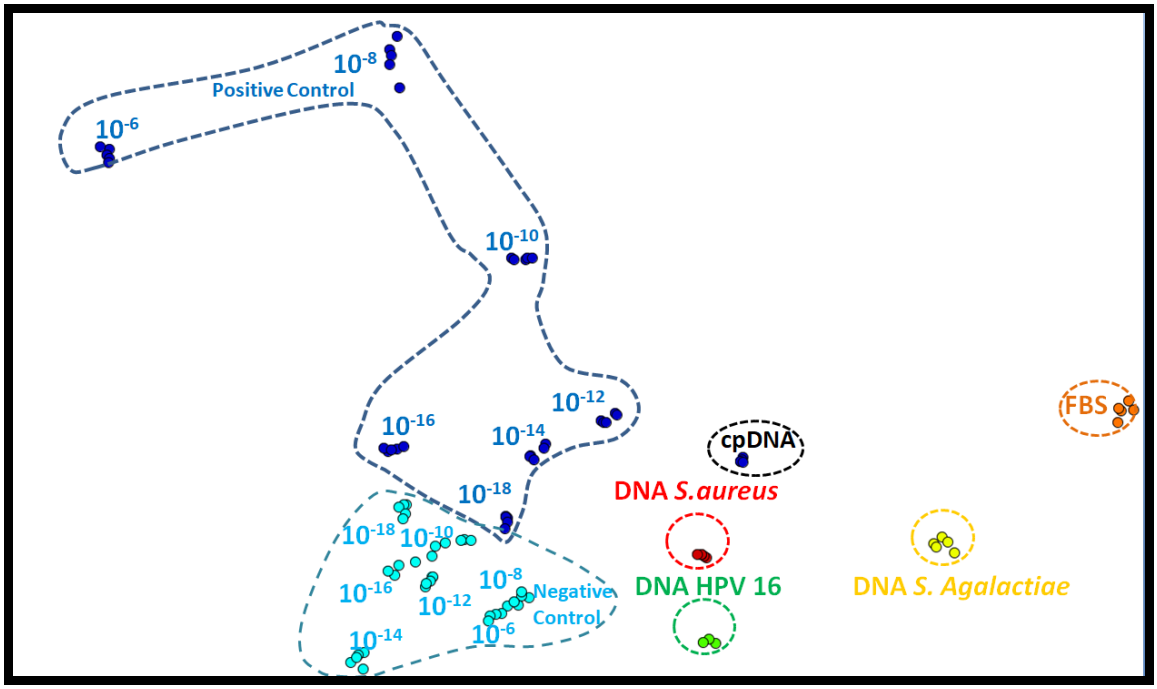

Figure 4. IDMAP projection of the capacitance spectra for samples with ssDNA SARS-CoV-2 at various concentrations, measured using genosensors constructed with 11-MUA SAM coated with an ssDNA SARS-CoV-2 probe. No false positives are observed, indicating that the mechanism governing SARS-CoV-2 detection occurs through specific interactions between the probe and the complementary sequence.

Detection using the same genosensor architecture was performed with electrochemical impedance spectroscopy, but its distinction ability was considerably lower, as indicated in the results in Figure S5 in the Supporting Information. In particular, the overall Silhouette Coefficient (*S*) value is considerably lower (S= -0.18) than for the measurements obtained with electrical impedance spectroscopy.

Optical Detection

Optical detection was carried out using the AuNp/glass plasmonic genosensor (Figure S3). A redshift in the transmitted LSPR spectrum was observed due to the hybridization between the cpDNA SARS-CoV-2 (probe) and the ssDNA SARS-CoV-2 complementary sequence, as indicated in Figure 5a for dilutions with PBS/$MgCl_2$ at concentrations between 1×10^{-10} and 1×10^{-6} mol L^{-1}. Figure 5b shows the change in the LSPR spectrum shift with increasing concentration of the complementary sequence. The dispersion in the data represents the standard error for different substrates for each concentration of the ssDNA sequence. The blank measurements represented the response of the genosensor to the pure PBS/$MgCl_2$ buffer solution and were repeated for ten devices resulting in the average peak shift $\Delta\lambda = 0.1$ nm, with an error of 0.15 nm. The selectivity of the genosensor was confirmed by performing detection tests with the non-complementary sequence. No shift in the LSPR spectrum was observed in the negative control detection tests, as plotted in the gray point in Figure 5a. The positive sequences could also be distinguished from the blank and the negative control sequence, as shown in the IDMAP plot in Figure S6.

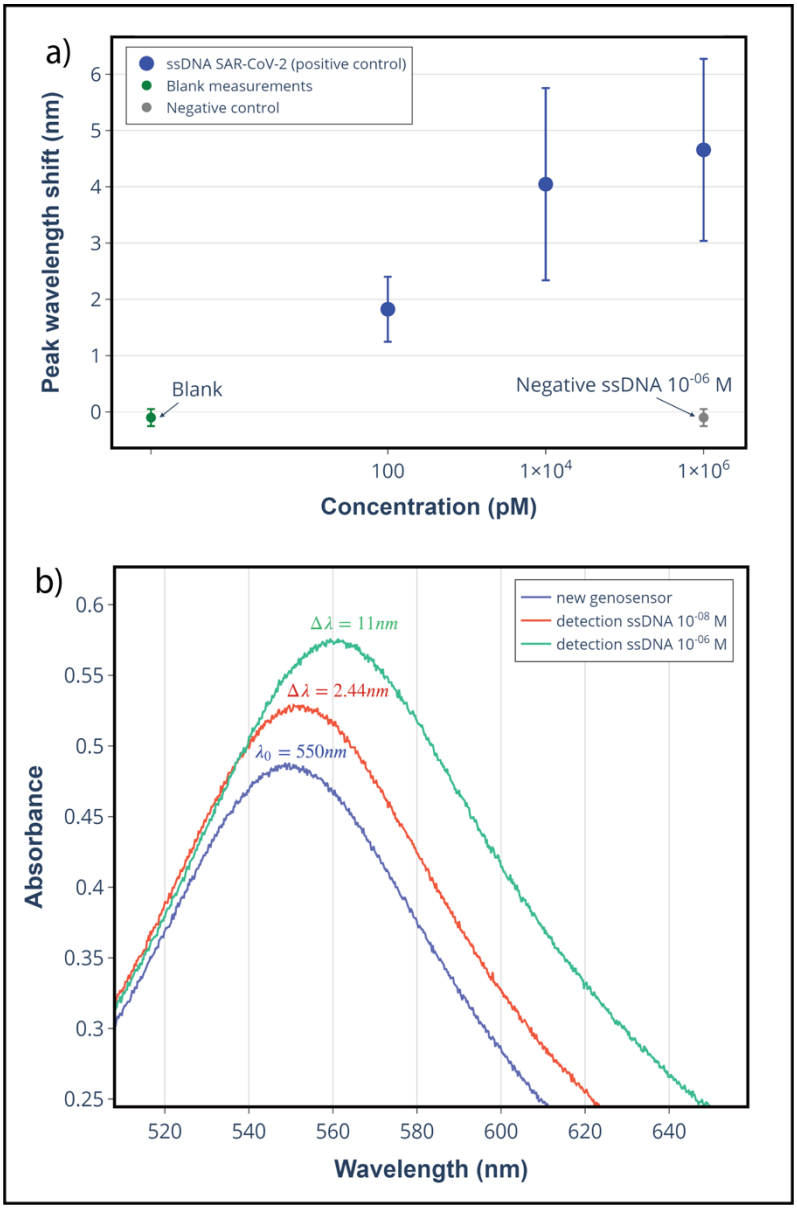

Figure 5.a) The LSPR peak shift for the detection tests performed with the optical genosensor. The blue points represent the sensitivity tests with the complementary sequence and the increase of the peak shift with the positive control ssDNA concentration. The green and the gray points represent the selectivity tests with pure PBS/MgCl2 (Blank) and with the non-complementary sequence, respectively. b) Measured LSPR spectrum before and after the interaction of the optical genosensor substrate with the solution containing the complementary sequence.

Adsorption Mechanism responsible for SARS-CoV-2 detection

The genosensors reported in this paper detected changes in electrical, electrochemical, and optical signals from interactions between the active layer

immobilized on 11-MUA films and synthetic ssDNA SARS-CoV-2. These changes can be investigated using PM-IRRAS, whose spectra are displayed in Figure 6. There is a considerable increase in the PM-IRRAS signal after hybridization for the antisymmetric PO_2^- dipole band at 1241 cm^{-1}[54] and the COOH band at 1735 cm^{-1}.[55,56] The PM-IRRAS spectra in Figures S7a and S7b in the Supporting Information confirm that exposure to any concentration of positive and negative DNA sequences for SARS-CoV-2 leads to changes. This should be expected owing to the nature of the PM-IRRAS technique that is sensitive not only to non-specific adsorption but also to changes in the orientation of molecules in the genosensor. Nevertheless, the signature generated by hybridization could be established.

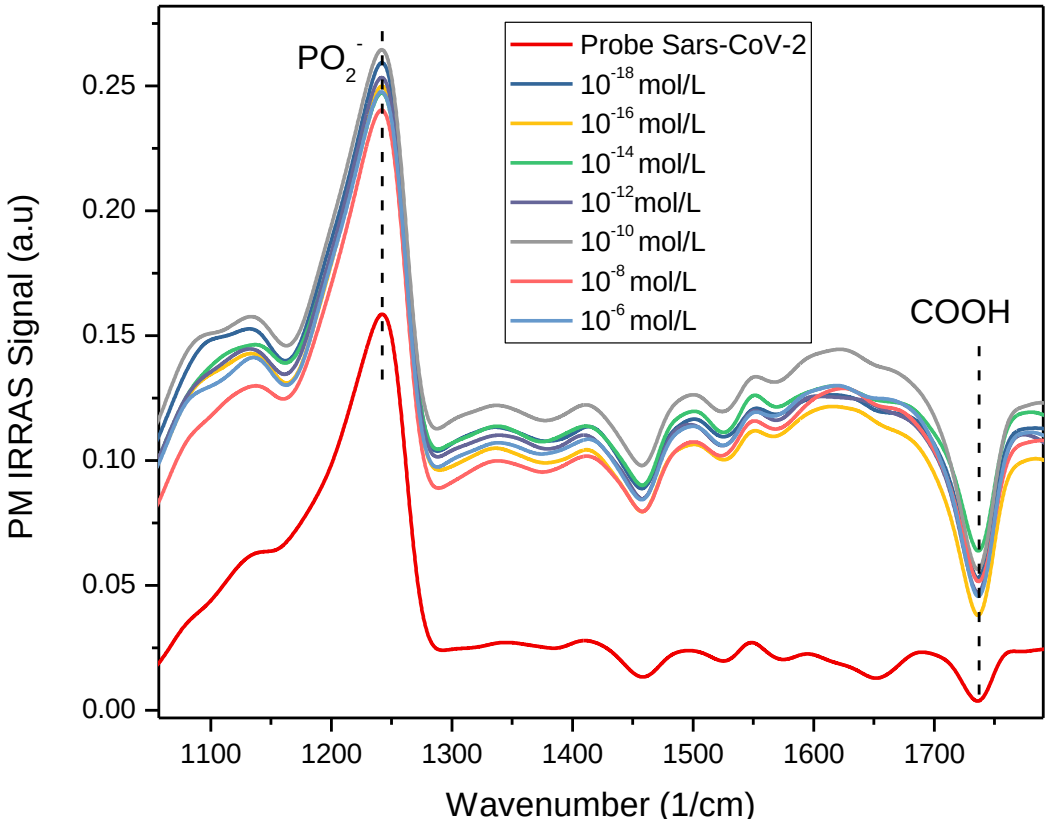

Figure 6. PM-IRRAS spectra for the 11-MUA/cpDNA genosensor before and after exposure to different concentrations of ssDNA SARS-CoV-2 positive sequences (complementary). Also shown in red trace is the spectrum for the genosensor exposed to PBS.

Diagnosis based on machine learning applied to image analysis of genosensors

Machine learning for image analysis is well established, but this applies to the imaging of biological samples. Image analysis of the sensing (or biosensing) units after exposure to biological samples is an embryonic topic, with a single previous contribution reported in the literature, to our best knowledge[57]. In the latter work, the SEM images of genosensors employed for a cancer biomarker had sufficient resolution to reveal nanoscopic structures. Using such high resolution was justified by a higher likelihood to distinguish the different samples since the detection mechanisms occur at the molecular level. The long-term goal, however, is to employ optical images from a standard microscope and ideally from a smartphone camera. This goal motivates our choice of employing low-resolution SEM images, with the smaller magnification (1,000X) being equivalent to that of optical microscopes.

The typical images of the genosensing units shown in Figure 1 were treated with non-supervised and supervised ML algorithms. In the supervised learning test, the classification task was performed in two datasets, which differ in the magnification of micrographs. The highest accuracy for both binary and multiclass cases was achieved using 1,000X images, as shown in Table 3 (the results for the magnification 10,000X are given in Table S2). It may appear surprising that better distinction was achieved with lower-resolution images. However, a visual inspection indicated that in several cases the images presented defects and artifacts of dimensions comparable to those of the objects observed with 10,000X magnification (some representative images are shown in Figure S8 in the Supporting information), which may have negatively affected the analysis. On the other hand, for the images with 1,000X, these defects were possibly sufficiently large for the machine learning algorithms to “learn” they were artifacts. The

visual analysis also revealed that the molecular-level interactions owing to hybridization are translated into evident changes in the morphology of the genosensors.

In the binary classification where the task is to separate the images of sensing units exposed to ssDNA SARS–CoV-2 concentrations (with all concentrations put together) from those which were not (negative and interferents), the highest accuracy was 99.66% (0.48) for the Fourier descriptors and the SVM classifier. Moreover, most image analysis methods yielded accuracy higher than 95% with LDA or SVM classifiers. In the multiclass classification, a distinction was made of the different concentrations of SARS–CoV-2, negative and interferent samples, totaling nine classes. The best results in Table 3 were obtained with CLBP (95.78% (0.97)) and LCFNN (91.36% (1.35)) features using the LDA classifier. Among the DCNN methods, DenseNet201 with LDA achieved the highest accuracy (94.48% (1.05)). These results suggest a substantial distinction between the different concentrations of SARS–CoV-2, negative, and interferent samples.

Table 3. Accuracy in binary and multiclass classifications of SEM images with 1,000X magnification.

Methods	Binary		Multiclass	
	LDA	SVM	LDA	SVM
AHP	92.30 (3.57)	98.28 (1.53)	90.12 (1.92)	87.73 (1.34)
CLBP	98.24 (1.28)	98.50 (1.10)	**95.78 (0.97)**	93.01 (0.93)
CNTD	93.78 (3.40)	96.50 (1.66)	89.77 (1.79)	83.91 (1.51)
GLDM	96.62 (2.15)	98.41 (0.94)	90.56 (1.17)	79.38 (1.49)
LCFNN	98.80 (0.49)	98.75 (0.46)	91.36 (1.35)	88.58 (1.03)
Fourier	95.77 (1.94)	**99.66 (0.48)**	77.55 (2.58)	72.57 (1.94)
Fractal	92.83 (3.28)	83.96 (3.12)	74.06 (2.43)	33.40 (2.29)
DenseNet201	99.14 (0.85)	99.21 (0.74)	94.48 (1.05)	90.23 (1.24)
InceptionResNetV2	98.50 (1.27)	98.46 (0.74)	86.87 (1.60)	79.41 (1.39)
MobileNet	98.54 (1.10)	98.67 (0.94)	89.12 (1.58)	87.20 (1.10)

We also performed experiments using an unsupervised learning technique. For qualitative analysis, we employed the t-distributed Stochastic Neighbor Embedding (t-SNE)[47], a multidimensional projection technique for visualizing high-dimensional data. Analogous to IDMAP (albeit using a different optimization strategy), it performs a dimensionality reduction to obtain a two-dimensional representation of the high-dimensional data points while attempting to preserve the distribution of the pairwise distances observed in the original space. Three of the best-handcrafted methods (features Fourier, CLBP, and LCFNN) and three DCNN were considered. The results in

Figure 7 indicate that all methods from clusters of similar samples, with a higher distinction between those with positive samples for SARS–CoV-2 or the remainder (negative and interferents). The DCNN MobileNet also shows promising performance, hence being a strong candidate for a mobile deep learning application of the proposed approach.

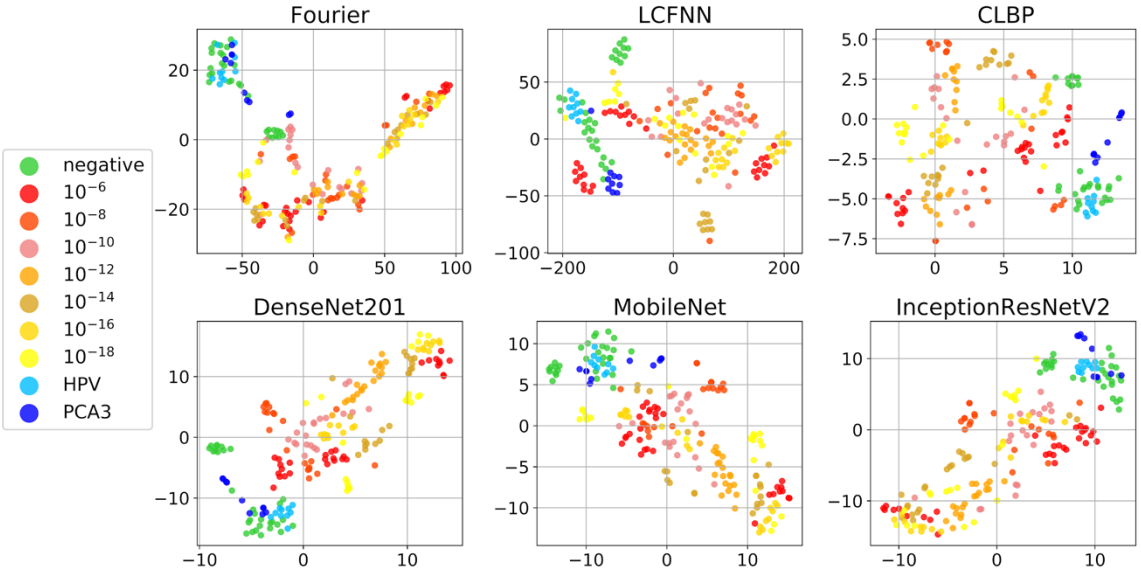

Figure 7. t-SNE 2D projections of SEM image features obtained with different methods.

For a quantitative analysis in a non-supervised scenario, we consider the well-known *k*-means clustering technique[31,39]. The experiment was performed using the Euclidean distance and 20 repetitions, as *k*-means has a random component in the initialization of its clusters. The Rand-Index was utilized as a measure of cluster quality. It measures the average similarities between clusters in a range between 0 and 1 (low to high similarity, respectively). Table 4 shows the Rand Index for the image analysis methods using all nine sample groups (k=9). The values achieved with several methods

indicate a good clustering of the data. Combined with the t-SNE projections, it further corroborates the results from the supervised learning experiment.

Table 4. Rand index for clusters computed with k-means using nine groups on the dataset with 1,000 magnification datasets.

Methods	Rand Index
AHP	0.83
CLBP	0.86
LCFNN	0.87
Fractal	0.81
Fourier	0.83
GLDM	0.81
DenseNet201	0.82
MobileNet	0.80
InceptionResNetV2	0.86

4. Conclusions

A genosensor has been developed which can detect an ssDNA sequence of SARS-CoV-2 considering different detection principles. The most sensitive method was impedance spectroscopy, which obtained a detection limit of 0.5 aM. This sensitivity corresponds to 0.3 copy/μL and should suffice to detect the SARS-CoV-2 sequence in saliva or other body fluids. That detection could be performed with electrochemical and optical methods techniques is a particularly relevant finding, for besides confirming the suitability of the genosensing architecture, it implies in versatility in the mode of operation. In particular, the hybridization between the complementary sequences

confirmed with PM-IRRAS measurements led to morphological changes on the genosensors, which could be captured in low-resolution SEM images. Upon applying supervised and non-supervised machine learning algorithms to image processing, we could obtain a high distinction accuracy between the different concentrations of SARS-CoV-2 ssDNA sequences. This capability opens multiple avenues for instrument-free detection of SARS-CoV-2 if an optical microscope can be coupled to smartphones. Judging by the analysis of the images, one may speculate that photos from smartphones can be used in the future, a supposition that requires further verification. In all the detection experiments, the selectivity of the genosensors was verified with control samples, including a negative sequence for SARS-CoV-2 and other DNA biomarkers not related to COVID-19.

The main limitation in this work is associated with the samples analyzed, as the suitability of the genosensor for diagnosis of SARS-CoV-2 in COVID-19 patients has not been tested. Based on the literature and our own previous experience with genosensors, we are hopeful that a sensitive, selective diagnosis will be possible. This confirmation will now be pursued by our team, and we also hope other authors will employ the strategies and genosensor architecture for developing efficient diagnostic methods.

Acknowledgments

The authors are thankful to CAPES (88887.510657/2020-00, 88887.364257/2019-00 and PROCAD #3007/2014), São Paulo Research Foundation (FAPESP) (2013/14262, 2016/01919-6, 2018/18953-8, 2018/19750-3,2018/22214-6, 2019/00101-8, 2019/13514-9, 2016/23763-8, 2019/07811-0, 2020/02938-0) INEO,

INCTBio grants (FAPESP 2014/50867-3) and CNPq(423952/2018-8, 465389/2014-7, and 401256/2020-0) for the financial support.The authors are grateful to Angelo Luiz Gobbi and Maria Helena de Oliveira Piazzetta (LMF/LNNano/CNPEM) for producing the Au electrodes.

Authors' Contributions

JCS – performed impedance spectroscopy measurements did statistical analysis with IDMAP, wrote the manuscript; ACS – performed impedance spectroscopy measurements, did statistical analysis with IDMAP and Parallel Coordinates, performed PM-IRRAS measurements and wrote the manuscript; VCR – performed PM-IRRAS measurements and SEM analysis, wrote the corresponding section in the manuscript; PRO – performed optical measurements and wrote the corresponding section in the manuscript; PAR – performed electrochemical impedance spectroscopy measurements and wrote the corresponding section; JLB - performed electrochemical impedance spectroscopy measurements and wrote the corresponding section; LAB – developed Simple-Z system and wrote the corresponding section; LDCC – did SEM analysis and wrote the corresponding section; LCR – performed machine learning studies and wrote the corresponding section; LS – performed machine learning studies and wrote the corresponding section; LCB – performed electrochemical impedance spectroscopy measurements; DSC – funding and analysis of impedance data; LHCM – funding, supervision and analysis of impedance data; MCFO – funding and analysis of computational treatment of the data; APLFC – funding and analysis of computational treatment of the data; EC – funding, supervision, and analysis of electrochemical impedance spectroscopy results; OMB – supervision and analysis of machine learning results; MEM – design of genosensors and analysis of detection of genetic material;

ONO – funding, supervision and coordination. All authors revised and approved the text.

References

(1) Mattioli, I. A.; Hassan, A.; Oliveira, O. N.; Crespilho, F. N. On the Challenges for the Diagnosis of SARS-CoV-2 Based on a Review of Current Methodologies. *ACS Sens.* **2020**, acssensors.0c01382. https://doi.org/10.1021/acssensors.0c01382.

(2) Singh, A.; Shaikh, A.; Singh, R.; Singh, A. K. COVID-19: From Bench to Bed Side. *Diabetes & Metabolic Syndrome: Clinical Research & Reviews* **2020**, *14* (4), 277–281. https://doi.org/10.1016/j.dsx.2020.04.011.

(3) Oliveira, B. A.; Oliveira, L. C. de; Sabino, E. C.; Okay, T. S. SARS-CoV-2 and the COVID-19 Disease: A Mini Review on Diagnostic Methods. *Rev. Inst. Med. trop. S. Paulo* **2020**, *62*, e44. https://doi.org/10.1590/s1678-9946202062044.

(4) Mahari, S.; Roberts, A.; Shahdeo, D.; Gandhi, S. *ECovSens-Ultrasensitive Novel In-House Built Printed Circuit Board Based Electrochemical Device for Rapid Detection of NCovid-19 Antigen, a Spike Protein Domain 1 of SARS-CoV-2*; preprint; Bioengineering, 2020. https://doi.org/10.1101/2020.04.24.059204.

(5) Bustin, S. A.; Nolan, T. RT-QPCR Testing of SARS-CoV-2: A Primer. *IJMS* **2020**, *21* (8), 3004. https://doi.org/10.3390/ijms21083004.

(6) Corman, V. M.; Landt, O.; Kaiser, M.; Molenkamp, R.; Meijer, A.; Chu, D. K.; Bleicker, T.; Brünink, S.; Schneider, J.; Schmidt, M. L.; Mulders, D. G.; Haagmans, B. L.; van der Veer, B.; van den Brink, S.; Wijsman, L.; Goderski, G.; Romette, J.-L.; Ellis, J.; Zambon, M.; Peiris, M.; Goossens, H.; Reusken, C.; Koopmans, M. P.; Drosten, C. Detection of 2019 Novel Coronavirus (2019-NCoV) by Real-Time RT-PCR. *Eurosurveillance* **2020**, *25* (3). https://doi.org/10.2807/1560-7917.ES.2020.25.3.2000045.

(7) Chu, D. K. W.; Pan, Y.; Cheng, S. M. S.; Hui, K. P. Y.; Krishnan, P.; Liu, Y.; Ng, D. Y. M.; Wan, C. K. C.; Yang, P.; Wang, Q.; Peiris, M.; Poon, L. L. M. Molecular Diagnosis of a Novel Coronavirus (2019-NCoV) Causing an Outbreak of Pneumonia. *Clinical Chemistry* **2020**, *66* (4), 549–555. https://doi.org/10.1093/clinchem/hvaa029.

(8) Holshue, M. L.; DeBolt, C.; Lindquist, S.; Lofy, K. H.; Wiesman, J.; Bruce, H.; Spitters, C.; Ericson, K.; Wilkerson, S.; Tural, A.; Diaz, G.; Cohn, A.; Fox, L.; Patel, A.; Gerber, S. I.; Kim, L.; Tong, S.; Lu, X.; Lindstrom, S.; Pallansch, M. A.; Weldon, W. C.; Biggs, H. M.; Uyeki, T. M.; Pillai, S. K. First Case of 2019 Novel Coronavirus in the United States. *N Engl J Med* **2020**, *382* (10), 929–936. https://doi.org/10.1056/NEJMoa2001191.

(9) Hosseini, A.; Pandey, R.; Osman, E.; Victorious, A.; Li, F.; Didar, T.; Soleymani, L. Roadmap to the Bioanalytical Testing of COVID-19: From Sample Collection to Disease Surveillance. *ACS Sens.* **2020**, *5* (11), 3328–3345. https://doi.org/10.1021/acssensors.0c01377.

(10) Nguyen, T.; Duong Bang, D.; Wolff, A. 2019 Novel Coronavirus Disease (COVID-19): Paving the Road for Rapid Detection and Point-of-Care Diagnostics. *Micromachines* **2020**, *11* (3), 306. https://doi.org/10.3390/mi11030306.

(11) Broughton, J. P.; Deng, X.; Yu, G.; Fasching, C. L.; Servellita, V.; Singh, J.; Miao, X.; Streithorst, J. A.; Granados, A.; Sotomayor-Gonzalez, A.; Zorn, K.; Gopez, A.; Hsu, E.; Gu, W.; Miller, S.; Pan, C.-Y.; Guevara, H.; Wadford, D. A.; Chen, J. S.;

Chiu, C. Y. CRISPR–Cas12-Based Detection of SARS-CoV-2. *Nat Biotechnol* **2020**, *38* (7), 870–874. https://doi.org/10.1038/s41587-020-0513-4.
(12) Lotfi, M.; Rezaei, N. CRISPR/Cas13: A Potential Therapeutic Option of COVID-19. *Biomedicine & Pharmacotherapy* **2020**, *131*, 110738. https://doi.org/10.1016/j.biopha.2020.110738.
(13) Bundschuh, C.; Egger, M.; Wiesinger, K.; Gabriel, C.; Clodi, M.; Mueller, T.; Dieplinger, B. Evaluation of the EDI Enzyme Linked Immunosorbent Assays for the Detection of SARS-CoV-2 IgM and IgG Antibodies in Human Plasma. *Clinica Chimica Acta* **2020**, *509*, 79–82. https://doi.org/10.1016/j.cca.2020.05.047.
(14) Alharbi, S. A.; Almutairi, A. Z.; Jan, A. A.; Alkhalify, A. M. Enzyme-Linked Immunosorbent Assay for the Detection of Severe Acute Respiratory Syndrome Coronavirus 2 (SARS-CoV-2) IgM/IgA and IgG Antibodies Among Healthcare Workers. *Cureus* **2020**. https://doi.org/10.7759/cureus.10285.
(15) Zuo, B.; Li, S.; Guo, Z.; Zhang, J.; Chen, C. Piezoelectric Immunosensor for SARS-Associated Coronavirus in Sputum. *Anal. Chem.* **2004**, *76* (13), 3536–3540. https://doi.org/10.1021/ac035367b.
(16) Fabiani, L.; Saroglia, M.; Galatà, G.; De Santis, R.; Fillo, S.; Luca, V.; Faggioni, G.; D'Amore, N.; Regalbuto, E.; Salvatori, P.; Terova, G.; Moscone, D.; Lista, F.; Arduini, F. Magnetic Beads Combined with Carbon Black-Based Screen-Printed Electrodes for COVID-19: A Reliable and Miniaturized Electrochemical Immunosensor for SARS-CoV-2 Detection in Saliva. *Biosensors and Bioelectronics* **2021**, *171*, 112686. https://doi.org/10.1016/j.bios.2020.112686.
(17) Orooji, Y.; Sohrabi, H.; Hemmat, N.; Oroojalian, F.; Baradaran, B.; Mokhtarzadeh, A.; Mohaghegh, M.; Karimi-Maleh, H. An Overview on SARS-CoV-2 (COVID-19) and Other Human Coronaviruses and Their Detection Capability via Amplification Assay, Chemical Sensing, Biosensing, Immunosensing, and Clinical Assays. *Nano-Micro Lett.* **2021**, *13* (1), 18. https://doi.org/10.1007/s40820-020-00533-y.
(18) Kaushik, M.; Sonia; Mahendru, S.; Tyagi, P.; Kukreti, S. Multiple Dimensions of Functional Relevance of Genosensors. *Integrated Ferroelectrics* **2017**, *185* (1), 134–143. https://doi.org/10.1080/10584587.2017.1370349.
(19) Abad-Valle, P.; Fernández-Abedul, M. T.; Costa-García, A. DNA Single-Base Mismatch Study with an Electrochemical Enzymatic Genosensor. *Biosensors and Bioelectronics* **2007**, *22* (8), 1642–1650. https://doi.org/10.1016/j.bios.2006.07.015.
(20) Hamidi-Asl, E.; Raoof, J. B.; Hejazi, M. S.; Sharifi, S.; Golabi, S. M.; Palchetti, I.; Mascini, M. A Genosensor for Point Mutation Detection of P53 Gene PCR Product Using Magnetic Particles. *Electroanalysis* **2015**, *27* (6), 1378–1386. https://doi.org/10.1002/elan.201400660.
(21) Soares, J. C.; Soares, A. C.; Rodrigues, V. C.; Melendez, M. E.; Santos, A. C.; Faria, E. F.; Reis, R. M.; Carvalho, A. L.; Oliveira, O. N. Detection of the Prostate Cancer Biomarker PCA3 with Electrochemical and Impedance-Based Biosensors. *ACS Appl. Mater. Interfaces* **2019**, *11* (50), 46645–46650. https://doi.org/10.1021/acsami.9b19180.
(22) Qiu, G.; Gai, Z.; Tao, Y.; Schmitt, J.; Kullak-Ublick, G. A.; Wang, J. Dual-Functional Plasmonic Photothermal Biosensors for Highly Accurate Severe Acute Respiratory Syndrome Coronavirus 2 Detection. *ACS Nano* **2020**, *14* (5), 5268–5277. https://doi.org/10.1021/acsnano.0c02439.
(23) Huang, L.; Ding, L.; Zhou, J.; Chen, S.; Chen, F.; Zhao, C.; Xu, J.; Hu, W.; Ji, J.; Xu, H.; Liu, G. L. One-Step Rapid Quantification of SARS-CoV-2 Virus Particles

via Low-Cost Nanoplasmonic Sensors in Generic Microplate Reader and Point-of-Care Device. *Biosensors and Bioelectronics* **2021**, *171*, 112685. https://doi.org/10.1016/j.bios.2020.112685.

(24) Djaileb, A.; Charron, B.; Jodaylami, M. H.; Thibault, V.; Coutu, J.; Stevenson, K.; Forest, S.; Live, L. S.; Boudreau, D.; Pelletier, J. N.; Masson, J.-F. *A Rapid and Quantitative Serum Test for SARS-CoV-2 Antibodies with Portable Surface Plasmon Resonance Sensing*; preprint; 2020. https://doi.org/10.26434/chemrxiv.12118914.

(25) Seo, G.; Lee, G.; Kim, M. J.; Baek, S.-H.; Choi, M.; Ku, K. B.; Lee, C.-S.; Jun, S.; Park, D.; Kim, H. G.; Kim, S.-J.; Lee, J.-O.; Kim, B. T.; Park, E. C.; Kim, S. I. Rapid Detection of COVID-19 Causative Virus (SARS-CoV-2) in Human Nasopharyngeal Swab Specimens Using Field-Effect Transistor-Based Biosensor. *ACS Nano* **2020**, *14* (4), 5135–5142. https://doi.org/10.1021/acsnano.0c02823.

(26) Harris, C. R.; Millman, K. J.; van der Walt, S. J.; Gommers, R.; Virtanen, P.; Cournapeau, D.; Wieser, E.; Taylor, J.; Berg, S.; Smith, N. J.; Kern, R.; Picus, M.; Hoyer, S.; van Kerkwijk, M. H.; Brett, M.; Haldane, A.; del Río, J. F.; Wiebe, M.; Peterson, P.; Gérard-Marchant, P.; Sheppard, K.; Reddy, T.; Weckesser, W.; Abbasi, H.; Gohlke, C.; Oliphant, T. E. Array Programming with NumPy. *Nature* **2020**, *585* (7825), 357–362. https://doi.org/10.1038/s41586-020-2649-2.

(27) Negri, L. H.; Vestri, C. *Lucashn/Peakutils: V1.1.0*; Zenodo, 2017. https://doi.org/10.5281/ZENODO.887917.

(28) Minghim, R.; Paulovich, F. V.; de Andrade Lopes, A. Content-Based Text Mapping Using Multi-Dimensional Projections for Exploration of Document Collections; Erbacher, R. F., Roberts, J. C., Gröhn, M. T., Börner, K., Eds.; San Jose, CA, 2006; p 60600S. https://doi.org/10.1117/12.650880.

(29) Paulovich, F. V.; Moraes, M. L.; Maki, R. M.; Ferreira, M.; Oliveira Jr., O. N.; de Oliveira, M. C. F. Information Visualization Techniques for Sensing and Biosensing. *Analyst* **2011**, *136* (7), 1344. https://doi.org/10.1039/c0an00822b.

(30) da Silva, N. R.; Van der Weeën, P.; De Baets, B.; Bruno, O. M. Improved Texture Image Classification through the Use of a Corrosion-Inspired Cellular Automaton. *Neurocomputing* **2015**, *149*, 1560–1572. https://doi.org/10.1016/j.neucom.2014.08.036.

(31) Rawat, W.; Wang, Z. Deep Convolutional Neural Networks for Image Classification: A Comprehensive Review. *Neural Computation* **2017**, *29* (9), 2352–2449. https://doi.org/10.1162/neco_a_00990.

(32) Weszka, J. S.; Dyer, C. R.; Rosenfeld, A. A Comparative Study of Texture Measures for Terrain Classification. *IEEE Trans. Syst., Man, Cybern.* **1976**, *SMC-6* (4), 269–285. https://doi.org/10.1109/TSMC.1976.5408777.

(33) Journaux, L.; Destain, M.-F.; Miteran, J.; Piron, A.; Cointault, F. Texture Classification with Generalized Fourier Descriptors in Dimensionality Reduction Context: An Overview Exploration. In *Artificial Neural Networks in Pattern Recognition*; Prevost, L., Marinai, S., Schwenker, F., Eds.; Lecture Notes in Computer Science; Springer Berlin Heidelberg: Berlin, Heidelberg, 2008; Vol. 5064, pp 280–291. https://doi.org/10.1007/978-3-540-69939-2_27.

(34) Backes, A. R.; Casanova, D.; Bruno, O. M. Texture Analysis and Classification: A Complex Network-Based Approach. *Information Sciences* **2013**, *219*, 168–180. https://doi.org/10.1016/j.ins.2012.07.003.

(35) Backes, A. R.; Casanova, D.; Bruno, O. M. PLANT LEAF IDENTIFICATION BASED ON VOLUMETRIC FRACTAL DIMENSION. *Int. J. Patt. Recogn. Artif. Intell.* **2009**, *23* (06), 1145–1160. https://doi.org/10.1142/S0218001409007508.

(36) Zhu, Z.; You, X.; Chen, C. L. P.; Tao, D.; Ou, W.; Jiang, X.; Zou, J. An Adaptive Hybrid Pattern for Noise-Robust Texture Analysis. *Pattern Recognition* **2015**, *48* (8), 2592–2608. https://doi.org/10.1016/j.patcog.2015.01.001.
(37) Zhenhua Guo; Lei Zhang; Zhang, D. A Completed Modeling of Local Binary Pattern Operator for Texture Classification. *IEEE Trans. on Image Process.* **2010**, *19* (6), 1657–1663. https://doi.org/10.1109/TIP.2010.2044957.
(38) Ribas, L. C.; Scabini, L. F. S.; Junior, J. J. de M. S.; Bruno, O. M. Learning Local Complex Features Using Randomized Neural Networks for Texture Analysis. *arXiv:2007.05643 [cs]* **2020**.
(39) Szegedy, C.; Ioffe, S.; Vanhoucke, V.; Alemi, A. Inception-v4, Inception-ResNet and the Impact of Residual Connections on Learning. *arXiv:1602.07261 [cs]* **2016**.
(40) Huang, G.; Liu, Z.; van der Maaten, L.; Weinberger, K. Q. Densely Connected Convolutional Networks. *arXiv:1608.06993 [cs]* **2018**.
(41) Howard, A. G.; Zhu, M.; Chen, B.; Kalenichenko, D.; Wang, W.; Weyand, T.; Andreetto, M.; Adam, H. MobileNets: Efficient Convolutional Neural Networks for Mobile Vision Applications. *arXiv:1704.04861 [cs]* **2017**.
(42) Deng, J.; Dong, W.; Socher, R.; Li, L.-J.; Kai Li; Li Fei-Fei. ImageNet: A Large-Scale Hierarchical Image Database. In *2009 IEEE Conference on Computer Vision and Pattern Recognition*; IEEE: Miami, FL, 2009; pp 248–255. https://doi.org/10.1109/CVPR.2009.5206848.
(43) Lin, M.; Chen, Q.; Yan, S. Network In Network. *arXiv:1312.4400 [cs]* **2014**.
(44) Cortes, C.; Vapnik, V. Support-Vector Networks. *Mach Learn* **1995**, *20* (3), 273–297. https://doi.org/10.1007/BF00994018.
(45) Webb, A. R.; Copsey, K. D. *Statistical Pattern Recognition*, 3rd ed.; Wiley: Hoboken, 2011.
(46) Flach, P. A. *Machine Learning: The Art and Science of Algorithms That Make Sense of Data*; Cambridge University Press: Cambridge ; New York, 2012.
(47) Maaten, L. van der; Hinton, G. Visualizing Data Using T-SNE. *Journal of Machine Learning Research* **2008**, *9*, 2579–2605.
(48) Lvovich, V. F. *Impedance Spectroscopy: Applications to Electrochemical and Dielectric Phenomena*; Wiley: Hoboken, N.J, 2012.
(49) *Impedance Spectroscopy: Theory, Experiment, and Applications*, 2nd ed.; Barsoukov, E., Macdonald, J. R., Eds.; Wiley-Interscience: Hoboken, N.J, 2005.
(50) Inselberg, A.; Dimsdale, B. Parallel Coordinates: A Tool for Visualizing Multi-Dimensional Geometry. In *Proceedings of the First IEEE Conference on Visualization: Visualization `90*; IEEE Comput. Soc. Press: San Francisco, CA, USA, 1990; pp 361–378. https://doi.org/10.1109/VISUAL.1990.146402.
(51) Soares, J. C.; Shimizu, F. M.; Soares, A. C.; Caseli, L.; Ferreira, J.; Oliveira, O. N. Supramolecular Control in Nanostructured Film Architectures for Detecting Breast Cancer. *ACS Appl. Mater. Interfaces* **2015**, *7* (22), 11833–11841. https://doi.org/10.1021/acsami.5b03761.
(52) Currie, L. A. Nomenclature in Evaluation of Analytical Methods Including Detection and Quantification Capabilities (IUPAC Recommendations 1995). *Pure and Applied Chemistry* **1995**, *67* (10), 1699–1723. https://doi.org/10.1351/pac199567101699.
(53) Laboratory Corporation of America. Emergency use authorization (USA) Summary COVID-19 RT-PCR Test. https://www.fda.gov/media/136151/download#:~:text=Limit%20of%20Detection%20(LoD)%20for,%2D%20CoV%2D2%20synthetic%20RNA (accessed Dec 9, 2020).

(54) Zelig, U.; Mordechai, S.; Shubinsky, G.; Sahu, R. K.; Huleihel, M.; Leibovitz, E.; Nathan, I.; Kapelushnik, J. Pre-Screening and Follow-up of Childhood Acute Leukemia Using Biochemical Infrared Analysis of Peripheral Blood Mononuclear Cells. *Biochimica et Biophysica Acta (BBA) - General Subjects* **2011**, *1810* (9), 827–835. https://doi.org/10.1016/j.bbagen.2011.06.010.
(55) Colthup, N. B.; Daly, L. H.; Wiberley, S. E. *Introduction to Infrared and Raman Spectroscopy*, 3rd ed.; Academic Press: Boston, 1990.
(56) *Vibrational Spectroscopy at Electrified Interfaces*; Więckowski, A., Korzeniewski, C., Braunschweig, B., Eds.; Wiley series on electrocatalysis and electrochemistry; Wiley: Hoboken, New Jersey, 2013.
(57) Rodrigues, V. C.; Soares, J. C.; Soares, A. C.; Braz, D. C.; Melendez, M. E.; Ribas, L. C.; Scabini, L. F. S.; Bruno, O. M.; Carvalho, A. L.; Reis, R. M.; Sanfelice, R. C.; Oliveira, O. N. Electrochemical and Optical Detection and Machine Learning Applied to Images of Genosensors for Diagnosis of Prostate Cancer with the Biomarker PCA3. *Talanta* **2021**, *222*, 121444. https://doi.org/10.1016/j.talanta.2020.121444.